

JWST/MIRI detection of [Ne V], [Ne VI], and [O IV] wind emission in the O9V star 10 Lacertae

DAVID R. LAW,¹ CALUM HAWCROFT,¹ LINDA J. SMITH,¹ ALEXANDER W. FULLERTON,¹ CHRISTOPHER J. EVANS,²
KARL D. GORDON,¹ NIMISHA KUMARI,³ AND CLAUS LEITHERER¹

¹Space Telescope Science Institute, 3700 San Martin Drive, Baltimore, MD, 21218, USA

²European Space Agency (ESA), ESA Office, Space Telescope Science Institute, 3700 San Martin Drive, Baltimore, MD 21218, USA

³AURA for European Space Agency (ESA), ESA Office, Space Telescope Science Institute, 3700 San Martin Drive, Baltimore, MD, 21218, USA

ABSTRACT

We report the detection of broad, flat-topped emission in the fine-structure lines of [Ne V], [Ne VI], and [O IV] in mid-infrared spectra of the O9 V star 10 Lacertae obtained with JWST/MIRI. Optically thin emission in these high ions traces a hot, low-density component of the wind. The observed line fluxes imply a mass-loss rate of $> 3 \times 10^{-8} M_{\odot} \text{ yr}^{-1}$, which is an order of magnitude larger than previous estimates based on UV and optical diagnostics. The presence of this hot component reconciles measured values of the mass-loss rate with theoretical predictions, and appears to solve the “weak wind” problem for the particular case of 10 Lac.

Keywords: stars: massive – stars: mass loss – stars: winds, outflows – stars: individual (10 Lacertae) – infrared: spectroscopy

1. INTRODUCTION

Mass loss via stellar winds is a critical component of the evolution of massive stars, but our understanding of such winds is incomplete. While theoretical models successfully predict the mass outflow rates from the most massive O-type stars, a sudden reduction in wind strength is observed below a threshold luminosity of $\log(L/L_{\odot}) \sim 5.2$. This so-called ‘weak-wind problem’ has been confirmed in multiple star-forming environments in the SMC (Bouret et al. 2003; Martins et al. 2004), LMC (Brands et al. 2022; Hawcroft et al. 2024), and the Milky Way (Martins et al. 2005; Marcolino et al. 2009; de Almeida et al. 2019) with a drop in observed mass-loss rates of around 2 orders of magnitude compared to theoretical predictions. Indeed, below this threshold luminosity all typical wind diagnostics become very weak or disappear completely, meaning that only upper limits on the mass-loss rates can be set.

It remains unclear whether the winds of massive stars in this low luminosity regime are truly so weak (which would impact evolutionary and feedback predictions), or whether they may simply not be visible in the traditional UV/optical wavelength regimes. If the winds are genuinely weak, theoretical solutions have been proposed suggesting a possible loss of line-driving force from the recombination of iron (Vink 2022), a decoupling of minor ions and the bulk winds (Owocki & Puls 2002), or simply an incomplete line-driving formalism (Lattimer & Cranmer 2021). Alternatively, since the low density outflows in O dwarfs result in inefficient cooling, it is possible that the winds from late-type O stars

could be shock heated to extremely high temperatures and diagnostics would thus be available at only higher ionization stages (Lucy 2012; Lagae et al. 2021). Such higher ionization stages would only be observable in the extreme-UV or X-ray regime, or in the mid-infrared via fine-structure lines.

10 Lacertae (10 Lac, HD 214680) is one of the most well-studied late O-type dwarfs, with a low projected rotational velocity of $v \sin(i) = 14 \text{ km s}^{-1}$ and a macroturbulent broadening of 43 km s^{-1} (Holgado et al. 2022). Given its narrow lines and bright visual magnitude ($V = 4.9$), 10 Lac is one of the primary classification standards for the O9 V type (Sota et al. 2011) and has often been used as a reference target in quantitative studies of O-type stars. Likewise, 10 Lac is a well established weak-wind star. Early mass-loss rate estimates from $H\alpha$ were not able to identify the low wind strength and set an upper limit of $\sim 10^{-7} M_{\odot} \text{ yr}^{-1}$ (Leitherer 1988). An additional, independent upper limit on the mass-loss rate of $\sim 10^{-7} M_{\odot} \text{ yr}^{-1}$ comes from a non-detection in the radio (Biegging et al. 1989; Vallée & Moffat 1985; Scherrer et al. 2007). UV analysis was only able to set a maximum wind velocity of $1070 \pm 50 \text{ km s}^{-1}$ from N V (Prinja et al. 1990). This wind velocity was further supported by the UV fit from Martins et al. (2004) but the mass-loss rate upper limit was revised down to $\sim 10^{-8} M_{\odot} \text{ yr}^{-1}$ in Herrero et al. (2002) with these authors and Martins et al. (2004) using $\sim 10^{-10}$ and $\sim 10^{-9} M_{\odot} \text{ yr}^{-1}$ in their respective best-fits.

Here we report the discovery of highly ionized, broad forbidden emission lines arising in the outer wind of 10 Lac, suggestive of an unusually hot wind component. Such broad,

flat-topped forbidden fine-structure lines have been observed before in the mid- and far-IR spectra of Wolf-Rayet stars such as γ^2 Velorum in the ionic species of [S IV], [Ne II], [Ne III] and [O III] (Barlow et al. 1988; Crowther et al. 2024). As shown by Barlow et al. (1988), the rectangular line profiles indicate that these features are optically thin and formed in the outer parts of the stellar wind, where the densities are low and the wind has reached its terminal velocity. Because of their simple formation conditions, the lines can be used as diagnostics to determine stellar properties such as abundances and mass loss rates.

We describe the observations and data processing techniques in §2, present the MIRI spectra and measurements in §3, and discuss the implications of these results in §4.

2. OBSERVATIONS AND DATA PROCESSING

We observed 10 Lac in July 2022 using the Mid-Infrared Instrument’s (MIRI) Medium Resolution Integral Field Unit Spectrometer (MRS; Argyriou et al. 2023) onboard the James Webb Space Telescope (JWST) as part of a Cycle 1 calibration program designed to refine the MRS geometric distortion solution (JWST Program ID [PID] 1524, PI: Law). This program selected 10 Lac as the target for its brightness, rich parallel imaging field for measuring absolute astrometry, and potential utility in characterizing the MRS fringe and photometric calibration due to its smooth and well characterized spectrum and lack of variability (see, e.g., Gordon et al. 2022).

A custom 57-point dither pattern was used to dither the source widely around the field of view. With an exposure time of 55 seconds per exposure to maximize the S/N ratio at long wavelengths, the total exposure time was thus approximately 0.9 hours per spectral band. In addition to serving as the basis of the current MRS distortion solution (Patapis et al. 2024), these observations of 10 Lac also underpin the MRS photometric calibration shortward of $18 \mu\text{m}$ (Law et al. 2024).

Even deeper observations of 10 Lac were obtained as a part of calibration PID 3779 (PI: Gasman) designed to assess the impact of sub-pixel positioning on the spectral fringing of the MRS (Gasman et al. 2023). This program obtained a 9-point raster scan around each of 8 primary dither locations, for a total of 72 exposures and an effective integration time of 5.5 hours per spectral band. These data were obtained in November 2023, approximately 16 months after the data from PID 1524.

Both sets of data were processed through the standard CALWEBB_DETECTOR1, CALWEBB_SPEC2, and CALWEBB_SPEC3 stages of the JWST calibration pipeline (Bushouse et al. 2024) using the default STScI pipeline note-

book for the MIRI MRS observing mode¹. We used the software and calibration reference files corresponding to pipeline Build 11.0; i.e., *jwst* software version 1.15.1 and calibration reference data context 1276. We used the default spectral extraction aperture with radius $r = 2$ times the PSF FWHM in Channels 1–3 (i.e., shortward of $18 \mu\text{m}$), but set $r = 1$ FWHM in Channel 4 (longward of $18 \mu\text{m}$) in order to minimize the impact of annular background subtraction errors on the source spectrum which is faint at these long wavelengths. We additionally included the optional pipeline steps that applied bad pixel replacement and a 1-d residual fringe correction to the extracted spectra (Kavanagh et al. 2024).

While 10 Lac is classified as a double/multiple star, the first companion is 5 magnitudes fainter in the optical and separated by approximately 1 arcminute, while the second companion is about 10 magnitudes fainter than 10 Lac and separated by 3.6 arcseconds (Mason et al. 2001). Both companions lie outside the FOV of the MRS.

3. RESULTS

Figure 1 shows the $5\text{--}26.5 \mu\text{m}$ spectrum of 10 Lac from program 1524 in Rayleigh-Jeans units. While some high-frequency artifacts from residual fringing are evident (e.g., around $12 \mu\text{m}$), the spectrum is generally smooth with a typical S/N per wavelength bin ranging from ~ 1000 at $\lambda = 5\text{--}18 \mu\text{m}$ to ~ 200 at $\lambda = 22 \mu\text{m}$ and ~ 30 longward of $\lambda = 25 \mu\text{m}$.

At the spectral resolving power of the MRS ($R \sim 4000$ at $5 \mu\text{m}$, $R \sim 1500$ at $25 \mu\text{m}$; Argyriou et al. 2023) we are able to detect numerous narrow H I and He II emission features. These features have a mean velocity of $-7.0 \pm 7.9 \text{ km s}^{-1}$ (consistent with the 10 Lac systemic velocity of -10 km s^{-1}) and a kinematic width of $\sigma_{\text{HI}} = 42 \pm 5 \text{ km s}^{-1}$ after correction for the instrumental line spread function. These lines are formed due to non-LTE effects in the stellar photosphere (Najarro et al. 2011). Both H I and He II emission lines are relatively weak, with most peaking at 10% or less of the continuum flux (with the exceptions of the H I 6-5, 7-6, and 8-7 transitions) and would have been difficult to detect at the $R \sim 600$ spectral resolution characteristic of prior Spitzer IRS observations (e.g., Marcolino et al. 2017, see their Fig. A3).

The most conspicuous features in the 10 Lac spectrum are four broad emission lines that we identify as [Ne VI], [Ne V], and [O IV] (see Table 1). These highly-ionized species have ionization potentials of up to 126 eV for Ne^{5+} suggestive of high gas temperatures. We show continuum-subtracted spectra zoomed in around each of these features in Figure 2, along with the continuum-subtracted CALSPEC (Bohlin et al. 2014, 2022) model spectra, which contain only photospheric features. The spectra obtained from both PID 1524

¹ <https://github.com/spacetelescope/jwst-pipeline-notebooks>

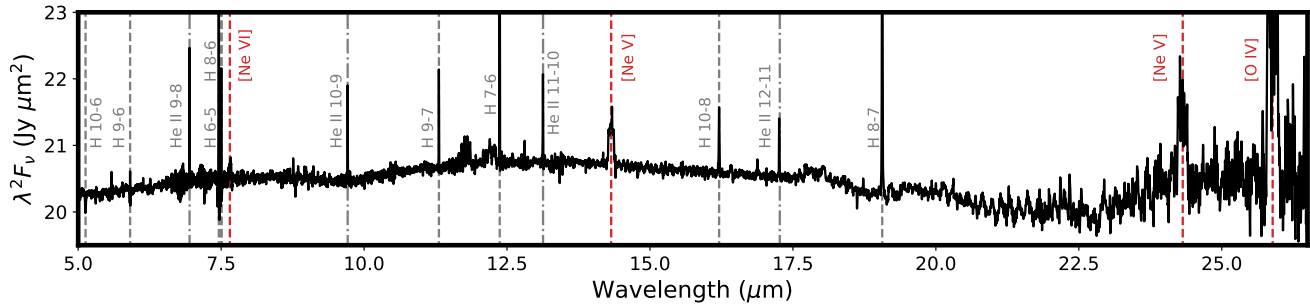


Figure 1. MIRI MRS spectrum of 10 Lac from PID 1524 plotted in Rayleigh-Jeans units. Dashed and dot-dashed vertical gray lines respectively indicate H I and He II photospheric emission features due to non-LTE effects, dashed red lines indicate highly ionized broad stellar wind [Ne VI], [Ne V], and [O IV] transitions. The extremely broad depression around $10\mu\text{m}$ is a known silicate dust absorption feature.

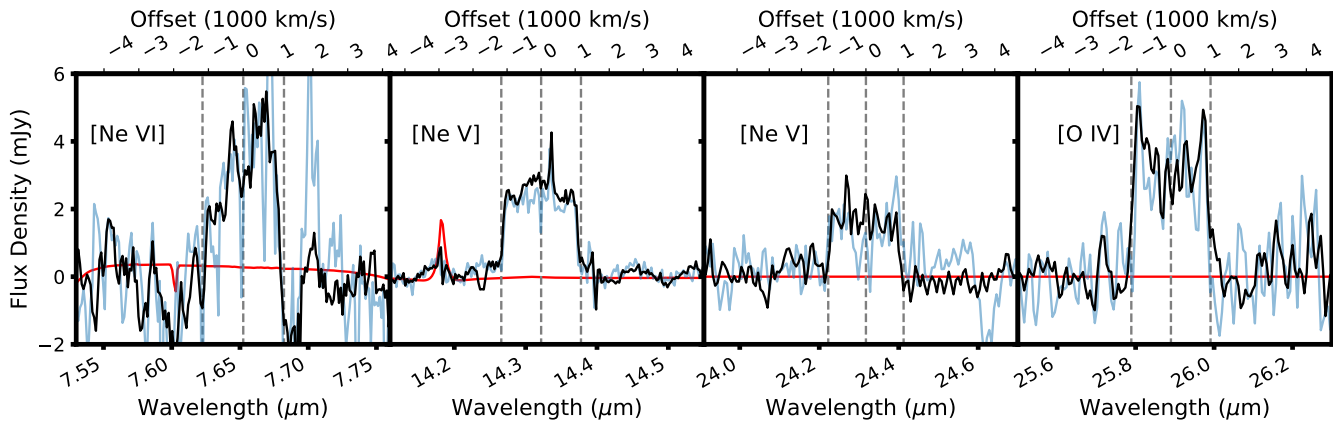


Figure 2. Continuum-subtracted spectrum of 10 Lac from PID 1524 (solid black line), zoomed in around the wavelengths of the broad [Ne VI], [Ne V], and [O IV] features. The light blue line shows the spectrum observed 16 months later by PID 3779 for comparison. The solid red line represents the corresponding continuum-subtracted CALSPEC model; the emission feature at $14.183\mu\text{m}$ is H I 13-9. Dashed vertical lines indicate $\pm 1170\text{ km s}^{-1}$ around the rest wavelength of each line.

and 3779 are consistent to within observational uncertainty. Despite the shorter integration times, the effective S/N ratio is higher in the PID 1524 spectra, likely because the 57-point dither marginalizes over flatfield systematics that may limit performance in PID 3779. Combining the data from both programs, we report integrated fluxes for each of these four lines in Table 1.

The [Ne V] lines in particular exhibit flat-topped profiles commonly seen in lower-ionization species² (which are not detected here) in Wolf-Rayet stars (Barlow et al. 1988; Crowther et al. 2024). Following Barlow et al. (1988), we measure the half-width at zero intensity and find an outflow speed of $1170 \pm 50\text{ km s}^{-1}$. This value agrees with the terminal wind velocity of 1070 km s^{-1} estimated by

² E.g., [S IV] $10.5\mu\text{m}$, [Ne II] $12.8\mu\text{m}$, [Ne III] $15.5\mu\text{m}$ with ionization potentials of 35 eV, 22 eV, and 41 eV respectively.

previous studies of the UV spectrum (Prinja et al. 1990; Martins et al. 2004). The [Ne VI] and [O IV] lines in contrast show evidence of structure, with [O IV] potentially being double-peaked with “horns” at $\pm 970\text{ km s}^{-1}$ with respect to the systemic velocity. As discussed by Ignace & Brimeyer (2006), the flat-topped profiles are indicative of a constant-velocity spherical stellar wind, while substructure in these profiles may be related to asymmetric winds and differences in the geometry of gas with different ionization energies (with horned profiles in particular resulting when the stellar wind is denser either at the poles or the equator).

4. DISCUSSION

In order to better understand the physical conditions in the stellar wind we aim to constrain the electron temperature (T_e) and density (n_e) in the fine-structure line-forming region. The [Ne V] $14.3\mu\text{m} / 24.3\mu\text{m}$ ratio is most sensitive to density across a wide range of temperatures (e.g., Sturm et al. 2002). Assuming a broad range of $T_e = 35\text{--}200\text{ kK}$ (with a lower limit of 35 kK set at the effective temperature of 10

Table 1. Parameters of Forbidden Emission Lines Detected in 10 Lac

Line	Rest Wavelength (μm)	Ionization Potential (eV)	Flux ($10^{-15} \text{ erg s}^{-1} \text{ cm}^{-2}$)	Critical Density ^a ($\log(n_e/\text{cm}^{-3})$)	Formation Radius (R_*)
[Ne VI]	7.6524	126	10.1 ± 0.5	6.0	60
[Ne V]	14.3217	97	3.80 ± 0.05	5.2	230
[Ne V]	24.3175	97	1.37 ± 0.06	5.0	275
[O IV]	25.890	55	2.94 ± 0.06	4.2	490

^a Assuming $T_e = 35 \text{ kK}$.

Lac from [Aschenbrenner et al. 2023](#)), the observed [Ne V] $14.3 \mu\text{m} / 24.3 \mu\text{m}$ ratio of 2.77 ± 0.13 corresponds to a density range $\log(n_e/\text{cm}^{-3}) = 4.5 - 5.0$, as shown in Figure 3. This range is broadly consistent with upper limits placed on n_e by the critical density³ n_c for the transitions. These are listed in Table 1 for $T_e = 35 \text{ kK}$; all of these values become much larger at higher electron temperatures.

Taking the equation of mass continuity as in [Smith & Houck \(2005\)](#) with n_c and assuming $\dot{M} = 3 \times 10^{-8} M_\odot \text{ yr}^{-1}$ (see below), we can calculate the radius at which the lines are formed assuming a smooth radial density profile; these are listed in Table 1 in terms of the stellar radius ($R_* = 7.4 R_\odot$, [Aschenbrenner et al. 2023](#)). We find that all the lines are formed below the critical density, at radii that are consistent with the wind having reached terminal velocity given a standard β acceleration profile.

IR forbidden fine-structure emission lines have often been used to determine abundances in the stellar winds of Wolf-Rayet stars, given that line strengths depend mainly on the wind strength and abundance ([Barlow et al. 1988](#); [Dessart et al. 2000](#); [Ignace et al. 2001](#); [Morris et al. 2004](#); [Smith & Houck 2005](#); [Crowther et al. 2024](#)). The ionic abundances γ_i of these types of line transitions depend on the mass-loss rate (\dot{M}) as $\gamma_i \propto \dot{M}^{-1.5}$. Therefore the lines we observe in the outer wind of 10 Lac can be used to put limits on \dot{M} for a given line flux I_{ul} , assumptions for T_e , n_e and knowledge of the distance and wind speed. We follow the methodology of [Barlow et al. \(1988\)](#), [Dessart et al. \(2000\)](#) and [Crowther et al. \(2024\)](#) and provide additional details, including the full expressions, in the Appendix.

In Figure 4 we show predictions for the ionisation fraction q (i.e., the fraction of atoms of a given element in a particular ionization state) using the measured line fluxes over a range of input mass-loss rates. We find that the trends in q with \dot{M} depend on T_e , but we can place lower limits on the mass-loss rate on the assumption that the entire neon and oxygen mass

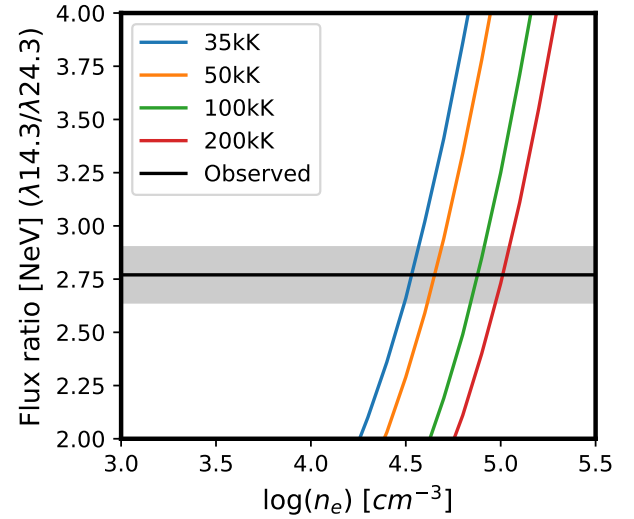


Figure 3. Flux ratios for [Ne V] $14.3 \mu\text{m} / 24.3 \mu\text{m}$ as a function of the electron temperature T_e and density n_e . Colored lines show model estimates produced using EQUIB ([Howarth & Adams 1981](#); [Danehkar 2020](#)) for values of T_e in the range 35-200 kK. The solid black line and grey shaded region show the measured flux ratio and 1σ uncertainty for 10 Lac, respectively.

budget is in the observed Ne^{4+} , Ne^{5+} , and O^{3+} ions. We find that \dot{M} cannot be below $\sim 10^{-8} M_\odot \text{ yr}^{-1}$ and is instead in the range $\dot{M} = 3 - 5 \times 10^{-8} M_\odot \text{ yr}^{-1}$ for $T_e \sim 35 \text{ kK}$ and in the range $\dot{M} = 4 - 7 \times 10^{-8} M_\odot \text{ yr}^{-1}$ for $T_e \sim 200 \text{ kK}$. These estimates are broadly within the range of theoretical mass-loss rates predicted by [Krtićka & Kubát \(2017\)](#) and [Vink et al. \(2000\)](#), and slightly larger than those predicted by [Björklund et al. \(2021\)](#).⁴

Since our observational estimates assume that the entire neon and oxygen mass budget is in the observed ions, any

³ At the critical density, spontaneous emissions equal collisional de-excitations for a given energy level.

⁴ A range of $\log(L/L_\odot)$ values have been quoted in the literature, with [Martins et al. \(2004\)](#) estimating a luminosity of 0.25 dex higher than our adopted value ([Aschenbrenner et al. 2023](#)); such a higher luminosity would correspond to a 0.55 dex increase in $\log(\dot{M})$ for all predicted mass-loss rates.

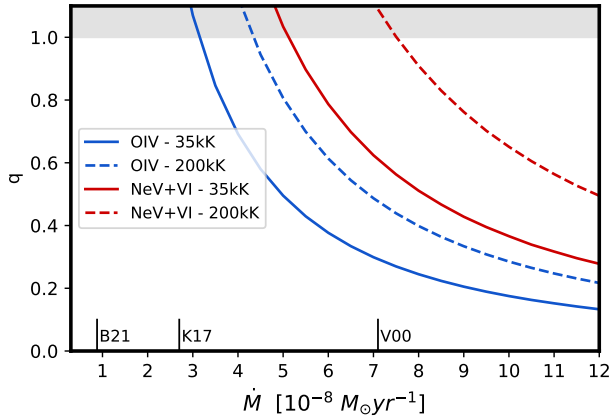


Figure 4. Ionisation fraction q as a function of mass-loss rate for O^{3+} (blue) and $Ne^{4+} + Ne^{5+}$ (red) ions. Solid and dashed lines show electron temperatures of $T_e = 35$ and 200 kK, respectively. Values of $q = 1$ represent the lower limit of the mass-loss rate for each curve assuming that the indicated ionization states comprise the total contribution of the respective element in the line-forming region. Values of $q > 1$ (grey shaded region) are thus unphysical, and any unaccounted-for species will drive $q < 1$. Vertical black ticks show theoretical mass-loss rate predictions from Björklund et al. (2021), B21, Krtička & Kubát (2017), K17 and Vink et al. (2000), V00.

unobserved species would drive q downwards, resulting in a higher total mass outflow rate. Regardless of the exact temperature and luminosity, the mass-loss rate estimated from the IR spectra is significantly higher than those determined from previous optical and UV analyses, and suggest that forbidden lines in the IR are better probes of the hot, low density wind regime than traditional optical diagnostics.

In Figure 5 we compare measured mass-loss rates as a function of luminosity for a sample of Galactic O stars compiled from the literature, along with the theoretical predictions of Vink et al. (2000) and Björklund et al. (2021). This comparison serves to highlight the discrepancy – the “weak-wind problem” – for stars with $\log(L/L_\odot) \lesssim 5.2$. Figure 5 also shows that – in stark contrast to previous determinations from optical and UV diagnostics – the mass-loss rate we estimate for 10 Lac from the [Ne v], [Ne vi], and [O iv] emission is in better agreement with theoretical predictions. It would appear that the resolution of the “weak-wind problem” for 10 Lac requires inclusion of a hot, low-density component that is difficult to detect with the diagnostics available in the optical and UV.

Hot, rarefied gas is a well-known by-product of the shocks produced by the potent line-deshadowing instability in line-driven stellar winds (Owocki et al. 1988). This shock-heated gas is generally thought to be the origin of X-rays from non-magnetic massive stars (see, e.g., Feldmeier 1995), and could also be responsible for the production of Ne^{4+} and

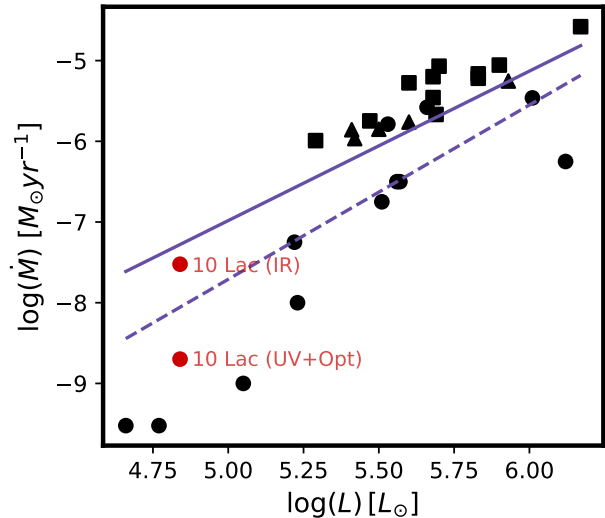


Figure 5. Mass-loss rates as a function of luminosity for Galactic O stars using results from Repolust et al. (2004); Martins et al. (2005); Crowther et al. (2006). Circles, triangles and squares correspond to luminosity classes V, III and I respectively. Solid and dashed lines show theoretical mass-loss rate predictions from Vink et al. (2000) and Björklund et al. (2021) respectively.

Ne^{5+} . Although it is traditionally assumed that the dense, “clumped” wind carries most of the mass, the current analysis for 10 Lac suggests that significant material also resides in the low-density, inter-clump medium. In this connection, the two-component phenomenological model developed by Lucy (2012) that assigns a larger volume to the hot, shocked gas than the cool, dense gas in the winds of low-luminosity stars merits consideration.

More observations of the mid-infrared fine-structure lines of highly ionized species with JWST/MIRI are clearly desirable to characterize the occurrence and behavior of these newly accessible diagnostics. A particular aim is to determine whether the presence of hot, rarefied gas is a general solution to the “weak-wind problem”, or if 10 Lac is a special case.

Initial indications are that the situation may be complicated. For example, Law et al. (2024) also observed the “weak-wind”, O9.5 V star μ Columbae as a MIRI calibrator. The MIRI spectrum of μ Col shows no evidence for the broad, high-ionization emission features seen in 10 Lac, despite the overall similarity of the fundamental stellar parameters of the two stars. Curiously, μ Col has a larger X-ray luminosity than 10 Lac (Berghoefer et al. 1996), which might suggest that it also has a wind with gas at even higher temperatures than in 10 Lac. By analyzing X-ray profiles, Huenemoerder et al. (2012) determined a mass-loss rate for μ Col that is consistent with theoretical predictions and much higher than what could be estimated from UV or optical di-

agnostics, thereby providing a potential solution to its weak-wind problem. The details of whether such winds are visible in the UV/optical, mid-infrared, or X-ray may therefore be intrinsically tied to the temperature and density profile of the winds and the most efficient radiation mechanisms available in each regime. Nonetheless, it appears likely that further observations of the fine-structure lines in the mid-infrared for a carefully selected sample of early-type stars will help to provide qualitatively new diagnostics that can allow us to better disentangle the nature of winds around massive stars.

This work is based on observations made with the NASA/ESA/CSA James Webb Space Telescope. The data were obtained from the Mikulski Archive for Space Telescopes at the Space Telescope Science Institute, which is operated by the Association of Universities for Research in Astronomy, Inc., under NASA contract NAS 5-03127 for JWST. These observations are associated with programs #1524 and #3779 and can be accessed via [doi: 10.17909/s1xy-k738](https://doi.org/10.17909/s1xy-k738).

REFERENCES

- de Almeida, E. S. G., Marcolino, W. L. F., Bouret, J.-C., et al. 2019, *A&A*, 628, A36
- Argyriou, I., Glasse, A., Law, D. R., et al. 2023, *A&A*, 675, A111. doi:10.1051/0004-6361/202346489
- Aschenbrenner, P., Przybilla, N. & Butler, K., 2023, *A&A*, 671, A36]
- Barlow, M. J., Roche, P. F., & Aitken, D. K. 1988, *MNRAS*, 232, 821. doi:10.1093/mnras/232.4.821
- Bieging, J. H., Abbott, D. C., & Churchwell, E. B. 1989, *ApJ*, 340, 518. doi:10.1086/167414
- Berghoefer, T. W., Schmitt, J. H. M. M., & Cassinelli, J. P. 1996, *A&AS*, 118, 481
- Björklund, R., Sundqvist, J. O., Puls, J., et al. 2021, *A&A*, 648, A36
- Bohlin, R. C., Gordon, K. D., & Tremblay, P.-E. 2014, *PASP*, 126, 711. doi:10.1086/677655
- Bohlin, R. C., Krick, J. E., Gordon, K. D., et al. 2022, *AJ*, 164, 10. doi:10.3847/1538-3881/ac6fe1
- Bouret, J.-C., Lanz, T., Hillier, D. J., et al. 2003, *ApJ*, 595, 1182
- Brands, S. A., de Koter, A., Bestenlehner, J. M., et al. 2022, *A&A*, 663, A36
- Bushouse, H., Eisenhamer, J., Dencheva, N., et al. 2024, Zenodo
- Crowther, P. A., Lennon, D. J., & Walborn, N. R. 2006, *A&A*, 446, 279
- Crowther, P. A., Barlow, M. J., Royer, P., et al. 2024, *MNRAS*, 528, 2026
- Danehkar, A. 2020, *The Journal of Open Source Software*, 5, 2798
- Dessart, L., Crowther, P. A., Hillier, D. J., et al. 2000, *MNRAS*, 315, 407
- Feldmeier, A. 1995, *A&A*, 299, 523
- Gasman, D., Argyriou, I., Sloan, G. C., et al. 2023, *A&A*, 673, A102. doi:10.1051/0004-6361/202245633
- Gordon, K. D., Gies, D. R., Schaefer, G. H., et al. 2018, *ApJ*, 869, 37
- Gordon, K. D., Bohlin, R., Sloan, G. C., et al. 2022, *AJ*, 163, 267. doi:10.3847/1538-3881/ac66dc
- Hawcroft, C., Mahy, L., Sana, H., et al. 2024, accepted in *A&A*, arXiv:2407.06775
- Herrero, A., Puls, J., & Najarro, F. 2002, *A&A*, 396, 949
- Barbá, R. H. et al. 2018, *A&A*, 613, A65
- Holgado, G., Simón-Díaz, S., Herrero, A. and Barbá, R. H., 2022, *A&A*, 665, A150
- Howarth, I. D. & Adams, S. 1981, University of London
- Huenemoerder, D. P., Oskinova, L. M., Ignace, R., et al. 2012, *ApJL*, 756, L34
- Ignace, R., Cassinelli, J. P., Quigley, M., et al. 2001, *ApJ*, 558, 771
- Ignace, R. & Brimeyer, A., 2006, *MNRAS*, 371, 343
- Kavanagh, P., et al., in prep.
- Krtićka, J. & Kubát, J. 2017, *A&A*, 606, A31
- Lagae, C., Driessen, F. A., Hennicker, L., et al. 2021, *A&A*, 648, A94
- Lattimer, A. S. & Cranmer, S. R. 2021, *ApJ*, 910, 48
- Law, D., Argyriou, I., Gordon, K.D., et al., *AJ* submitted, arXiv:2409.15435
- Leitherer, C. 1988, *ApJ*, 326, 356
- Leitherer, C., Chapman, J. M., & Koribalski, B. 1995, *ApJ*, 450, 289
- Lucy, L. B. 2012, *A&A*, 544, A120
- Luridiana, V., Morisset, C., & Shaw, R. A. 2015, *A&A*, 573, A42. doi:10.1051/0004-6361/201323152
- Marcolino, W. L. F., Bouret, J.-C., Martins, F., et al. 2009, *A&A*, 498, 837
- Marcolino, W. L. F., Bouret, J.-C., Lanz, T., et al. 2017, *MNRAS*, 470, 2710
- Martins, F., Schaerer, D., Hillier, D. J., et al. 2004, *A&A*, 420, 1087. doi:10.1051/0004-6361:20034509
- Martins, F., Schaerer, D., Hillier, D. J., et al. 2005, *A&A*, 441, 735
- Mason, B. D., Wycoff, G. L., Hartkopf, W. I., et al. 2001, *AJ*, 122, 3466. doi:10.1086/323920
- Morris, P. W., Crowther, P. A., & Houck, J. R. 2004, *ApJS*, 154, 413
- Najarro, F., Hanson, M. M., & Puls, J. 2011, *A&A*, 535, A32
- Owocki, S. P., Castor, J. I., & Rybicki, G. B. 1988, *ApJ*, 335, 914. doi:10.1086/166977
- Owocki, S. P. & Puls, J. 2002, *ApJ*, 568, 965

- Patapis, P., Argyriou, I., Law, D. R., et al. 2024, A&A, 682, A53.
doi:10.1051/0004-6361/202347339
- Prinja, R. K., Barlow, M. J., & Howarth, I. D. 1990, ApJ, 361, 607
- Repolust, T., Puls, J., & Herrero, A. 2004, A&A, 415, 349
- Schnerr, R. S., Rygl, K. L. J., van der Horst, A. J., et al. 2007, A&A, 470, 1105
- Smith, J.-D. T. & Houck, J. R. 2005, ApJ, 622, 1044
- Sota, A., Maíz Apellániz, J., Walborn, N. R et al. 2011, ApJS, 193, 24
- Sturm, E., Lutz, D., Verma, A., et al. 2002, A&A, 393, 821.
doi:10.1051/0004-6361:20021043
- Vallée, J. P., & Moffat, A. F. J. AJ, 90, 315. doi: 10.1086/113733
- Vink, J. S., de Koter, A., & Lamers, H. J. G. L. M. 2000, A&A, 362, 295
- Vink, J. S. 2022, ARA&A, 60, 203

APPENDIX

A. MASS-LOSS RATE CALCULATION

We estimate the mass loss rate from the observed emission line flux by combining continuity equations with our knowledge of the stellar atmospheric composition of 10 Lac. The fractional ionic abundance γ_i of a given element (Z) is defined as

$$\gamma_i \equiv \left(\frac{N_Z}{N_H + N_{He} + N_C + N_N + N_O + \dots} \right) \quad (\text{A1})$$

where N_Z is the number fraction in a given element, corresponding to an ionisation fraction q_i for a given element

$$q_i = \frac{\gamma_i}{\frac{N_Z}{N_H} \mu X_H} \quad (\text{A2})$$

where the total ionisation q is the sum of all contributing ionisation fractions $q = \sum_i q_i = 1$. μ is the mean ionic mass ($\mu = \sum \gamma_i m_i / \sum \gamma_i$) and is commonly around 1.5-1.6 for O-type stars. We adopt the photospheric abundances of each element for 10 Lac (e.g., $X_H = 0.725$, $X_{Ne} = 2.5 \times 10^{-3}$, $X_O = 6.8 \times 10^{-3}$) from [Aschenbrenner et al. \(2023\)](#), and assume that these relative abundances remain constant throughout the surrounding stellar wind.

The fractional ionic abundance γ_i can also be computed with an integral of the observed emission line flux over the line forming region surrounding the star (parameterized in terms of either the radius or the electron density) for a given atomic transition. Assuming the case of a stellar wind following an r^{-2} density law outflowing at fixed velocity $v_\infty = 1170 \text{ km s}^{-1}$, equations 5 and 6 of [Crowther et al. \(2024\)](#)⁵ together give

$$\gamma_i = \frac{(4\pi\mu m_H v_\infty)^{1.5}}{\ln(10)\dot{M}^{1.5}} \frac{2d^2 I_{ul}}{\sqrt{\gamma_e} A_{ul} h \nu_{ul}} \left(\int_0^\infty \frac{f_u(N_e, T_e)}{\sqrt{N_e}} d \log(N_e) \right)^{-1} \quad (\text{A3})$$

where γ_e is the mean number of electrons per ion which is commonly 0.8-1.0 for O-type stars (e.g. [Leitherer et al. 1995](#)). Likewise, m_H is the mass of hydrogen, h is Planck's constant, A_{ul} is the Einstein coefficient (taken from NIST), and ν_{ul} is the frequency of the line transition. $f_u(N_e, T_e)$ is the fraction of ions in the upper level for the atomic transition in question and is calculated using the EQUIB code ([Howarth & Adams 1981](#); [Danekhar 2020](#)) in the range of $N_e = 10^1 - 10^{12}$ for a given T_e , following [Dessart et al. \(2000\)](#) and [Crowther et al. \(2024\)](#). d is the distance to 10 Lac, which we take as 542 pc following [Aschenbrenner et al. \(2023\)](#).

Combining equations A1 and A3, it is therefore possible to infer a mass-loss rate \dot{M} as a function of the line flux I_{ul} in each observed [Ne V], [Ne VI], and [O IV] transition.

We note that the most common simple clumping models for stellar winds (as discussed by, e.g., [Dessart et al. 2000](#); [Crowther et al. 2024](#)) assume that line emission arises in the cooler, overdense clumps. This assumption is incompatible with emission from extremely highly ionized species such as [Ne VI] which is more likely to be produced in the hot interclump medium instead (e.g., [Lucy 2012](#)). Such clumping models are therefore not directly applicable to our observations, and we instead assume a smooth wind profile, deferring detailed consideration of multi-component winds to future work.

⁵ See also full derivation by [Dessart et al. \(2000\)](#).